Microsc. Microanal. 14, 36–47, 2008
DOI: 10.1017/S1431927608080161

Microscopy AND Microanalysis

© MICROSCOPY SOCIETY OF AMERICA 2008

Spatial Resolution and Information Transfer in Scanning Transmission Electron Microscopy

Yiping Peng, Mark P. Oxley,* Andrew R. Lupini, Matthew F. Chisholm, and Stephen J. Pennycook

Materials Science and Technology Division, Oak Ridge National Laboratory, Oak Ridge, TN 37831-6031, USA

Abstract: The relation between image resolution and information transfer is explored. It is shown that the existence of higher frequency transfer in the image is just a necessary but not sufficient condition for the achievement of higher resolution. Adopting a two-point resolution criterion, we suggest that a 10% contrast level between two features in an image should be used as a practical definition of resolution. In the context of scanning transmission electron microscopy, it is shown that the channeling effect does not have a direct connection with image resolution because sharp channeling peaks do not move with the scanning probe. Through a quantitative comparison between experimental image and simulation, a Fourier-space approach is proposed to estimate defocus and sample thickness. The effective atom size in Z-contrast imaging depends on the annular detector's inner angle. Therefore, an optimum angle exists for the highest resolution as a trade-off between reduced atom size and reduced signal with limited information transfer due to noise.

Key words: ADF, STEM, resolution, information transfer, noise, defocus, thickness, detector inner angle

Introduction

Motivated by the desire for single-atom sensitivity in imaging and analysis, microscopists have conducted an enduring pursuit for achieving higher resolution. Instrumental improvements in electron microscopy, especially the breakthrough brought by the practical correction of electron optical aberrations, have enabled experimental observations down to the atomic scale and even to the sub-Ångström level (Scherzer, 1949; Haider et al., 1998; Dellby et al., 2001; Krivanek et al., 2003; Nellist et al., 2004). Meanwhile, "what is resolution?" becomes a revived yet sometimes still controversial question. In this article we will restrict the discussion to spatial resolution, as distinguished from similar concepts like energy resolution or angular resolution applied for different observation techniques. Resolution or resolving power is the ability to determine if an image feature represents distinct objects rather than one object. Naturally, the spatial resolution of a microscope should be defined by the minimum distance between objects that are distinguishable in the image (e.g., O'Keefe & Allard, 2004). Resolution should be treated on a "seeing is believing" footing, and it is a property that is only meaningful with reference to an image. It is worth bearing in mind the difference between resolving and refining a structure; the concept of resolution should not be confused with precision or accuracy for parameter estimation, which can readily go beyond sub-Ångström in some measurement techniques (e.g., van Dyck et al., 2004). In more general usage, resolution is often defined by the number of dots per inch or pixels per line, obviously different from our subject here, which refers to the absolute resolvable distance and has the dimension of length.

The simplest case is the two-point resolution, that is, a system's ability to resolve two point sources of equal size and intensity, which has been widely used as a measure of the resolving capability of an imaging system. For this purpose, single-element systems with diamond cubic structures are suitable because they contain pairs of atomic columns, known as "dumbbells," when viewed along the $\langle 11m \rangle$ directions, where $m = 2n$ for $n = 0,1,2,3\ldots$ (O'Keefe et al., 2005). These physically stable structures with well-characterized lattice parameters serve suitably as test specimens for the high-resolution transmission electron microscope (TEM). Because the point spread function of an imaging instrument would generate blurred images of the dumbbell structures, a standard is needed to judge if a dumbbell is resolved or not: a yes or no problem. Of all the proposed two-point resolution criteria, the classical Rayleigh criterion (Rayleigh, 1879), which was derived with the central maximum of the image pattern for one point object falling on the first minimum for the other, is certainly the most famous. It is worth noting, however, that the Rayleigh criterion is an empirical estimate of resolution based on the assumption of the human visual system and may underestimate the resolving power of modern optical systems equipped

Received July 11, 2007; Accepted August 7, 2007.
*Corresponding author. E-mail: Oxleymp@ornl.gov

with state-of-the-art sensors. Rayleigh said this about his criterion: "This rule is convenient on account of its simplicity; and it is sufficiently accurate in view of the necessary uncertainty as to what exactly is meant by resolution" (Rayleigh, 1879). The Sparrow resolution (Sparrow, 1916), which states that the smallest resolvable distance between two point objects is that for which the minimum at the center begins to disappear, is clearly an upper limit, as the two objects are strictly not separated. An unambiguous definition of resolution can be difficult (den Dekker & van den Bos, 1997). However, because two points separated by an amount between the Rayleigh and Sparrow distances can be resolved to a certain degree, it seems appropriate for microscopists to use a criterion in between. For this purpose a concept of "resolution quality" was introduced and described by a Rayleigh–Sparrow parameter taking a value between one and zero (O'Keefe et al., 2005).

Information transfer in an image is closely related to but distinct from the resolution. Little has been done to clarify the relation between these two concepts. In this article we begin with a discussion in reciprocal space to show that higher frequency transfer in the image is a necessary but not sufficient condition for the achievement of higher resolution, as suggested by O'Keefe and Allard (2004). Although derived in the context of a scanning TEM (STEM), this conclusion has more general significance. The two-point resolution is then considered from the probe-shape point of view, followed by a demonstration using an experimental image of Si ⟨112⟩, and a dip contrast of 10% is proposed as a feasible resolution criterion. Based on a quantitative comparison of simulation with experiment, a Fourier-space approach to the estimation of defocus and sample thickness is presented. Finally the ultimate resolution limit and effective information transfer in the presence of noise are discussed.

Materials and Methods

Experimental

Direct sub-Ångström resolution has previously been demonstrated using a single-crystal Si sample oriented with the optical axis parallel to the ⟨112⟩ direction (Nellist et al., 2004). The annular-dark-field (ADF) image resolved Si columns separated by 0.78 Å and demonstrated information transfer to approximately 0.61 Å. We use this image as a test case for the discussion that follows. The ADF image was recorded using a VG Microscopes HB603U 300-kV dedicated STEM at the Oak Ridge National Laboratory (ORNL) that is fitted with a Nion aberration corrector. The ADF detector used had an inner semi-angle of 90 mrad, and a probe-forming aperture with semi-angle $\alpha = 22$ mrad was used. For the simulations that follow we have used typical parameters for the aberration-corrected probe: third-order spherical aberration $C_s = -0.037$ mm and fifth-order spherical aberration $C_5 = 100$ mm. All the image simulations in this article are performed using a Bloch-wave or multislice implementation (Findlay et al., 2003) of the cross-section formulation for incoherent lattice imaging (Allen et al., 2003).

Theory

Transfer Function for Incoherent STEM Imaging

In a STEM, an electron lens before the specimen focuses a coherent electron beam to form a small probe. The convergent probe is scanned over the specimen, and electrons exiting from the specimen are detected as a function of the two-dimensional probe position, $\mathbf{R}_0$. An incoherent Z-(atomic number) contrast image can be formed using an ADF detector. In optics it is often convenient to write real and reciprocal space vectors in their components perpendicular and parallel to the optic axis, thus $\mathbf{r} = (\mathbf{R}, z)$ and $\mathbf{k} = (\mathbf{K}, k_z)$. In the x–y plane defined by the defocus, the wave function of the STEM probe focused at $\mathbf{R}_0$, $P(\mathbf{R} - \mathbf{R}_0)$, can be written as a superposition of partial plane waves in the illuminating cone modulated by the lens aberration function $\chi(\mathbf{K})$:

$$P(\mathbf{R} - \mathbf{R}_0) = \int O(\mathbf{K}) \exp[i\chi(\mathbf{K})] \exp[i2\pi\mathbf{K}\cdot(\mathbf{R} - \mathbf{R}_0)]\, d\mathbf{K}. \tag{1}$$

Here $\mathbf{K}$ is the transverse wave vector of the incident partial plane wave and $O(\mathbf{K})$ is a circular top-hat function:

$$O(\mathbf{K}) = \begin{cases} 1 & \text{for } |\mathbf{K}| \le K_{\max} \\ 0 & \text{for } |\mathbf{K}| > K_{\max} \end{cases}, \tag{2}$$

where $K_{\max}$ is the radius of the objective aperture. The round coherent aberrations of the probe-forming optics are described by

$$\chi(\mathbf{K}) = \pi\Delta f\lambda|\mathbf{K}|^2 + \frac{\pi}{2} C_s \lambda^3 |\mathbf{K}|^4 + \frac{\pi}{6} C_5 \lambda^5 |\mathbf{K}|^6 + \cdots, \tag{3}$$

where we use the convention $\lambda = 1/|\mathbf{k}|$ and $\mathbf{k}$ is the wave vector of the incident electron. The aberrations considered here are Δf, C_s, and C_5, though higher order nonround terms may be added.

For perfectly incoherent imaging, the optical transfer function (OTF) is the Fourier transform of the system's intensity pointspread function. In the STEM case, the Fourier transform of $|P(\mathbf{R} - \mathbf{R}_0)|^2$ with respect to $\mathbf{R}$ gives the OTF as a function of spatial frequency, $\mathbf{p}$:

$$\mathrm{OTF}(\mathbf{p}) = \exp[-i2\pi\mathbf{p}\cdot\mathbf{R}_0]\int O^*(\mathbf{K})O(\mathbf{K}+\mathbf{p}) \times \exp[-i\chi(\mathbf{K})]\exp[i\chi(\mathbf{K}+\mathbf{p})]\,p\mathbf{K}, \quad (4)$$

where we have used

$$\int \exp(i2\pi\mathbf{K}\cdot\mathbf{R})\exp(-i2\pi\mathbf{K}'\cdot\mathbf{R})\exp(-i2\pi\mathbf{p}\cdot\mathbf{R})\,d\mathbf{R} = \delta(\mathbf{K}-\mathbf{K}'-\mathbf{p}). \quad (5)$$

Note that because there is no probe scanning involved so far, the $\mathbf{R}_0$-related exponential term remains in equation (4) as a planar phase ramp and does not affect the amplitude of the OTF. Due to the definition of the top-hat function in equation (2), the term $O^*(\mathbf{K})O(\mathbf{K}+\mathbf{p})$ reveals that the cutoff frequency of the OTF will be twice the probe-forming aperture radius, and this cutoff is independent of the lens aberrations and defocus contained in $\chi(\mathbf{K})$. These aberrations, however, determine the shape of the transfer function. In addition, because $\mathrm{OTF}(\mathbf{p}=\mathbf{0}) = \int O^*(\mathbf{K})O(\mathbf{K})\,d\mathbf{K}$, the OTF at zero spatial frequency is equal to the area of the probe-forming aperture and is proportional to the beam intensity.

Let us now consider the information transfer to an incoherent STEM image formed with transmitted electrons. An analytical examination can be carried out in the dynamical theory of electron diffraction by a crystal. Using a Bloch-wave formulation, the STEM image formed by incoherent (inelastic) scattering from a sample of thickness t may be written as a function of probe position $\mathbf{R}_0$ as (Allen et al., 2003)

$$\sigma_{\mathrm{dyn}}(\mathbf{R}_0,t) = \sum_{i,j} B^{ij}(\mathbf{R}_0,t)\sum_{\mathbf{g},\mathbf{h}} C^i_{\mathbf{g}} C^{j*}_{\mathbf{h}}\,\mu_{\mathbf{h},\mathbf{g}}. \quad (6)$$

This equation describes the contribution to the ADF image due to the interaction of the elastically scattered probe wavefunction (suitably attenuated by absorptive processes such as thermal diffuse scattering) with the inelastic (ADF) scattering potential. The contribution to the image from electrons that have been "absorbed" from the elastic beam is minimal for crystal lattices containing only light elements such as silicon. We have compared the results of Bloch-wave simulations with those obtained using a frozen phonon model (Kirkland, 1998) and found them to be in excellent agreement for the range of simulations considered here, as already indicated by Findlay et al. (2003). The indices i, j label the Bloch states, and the $C^i_{\mathbf{g}}$ are the Bloch-wave coefficients, where $\mathbf{g}$ is a reciprocal space vector. For plane-wave illumination, the vector $\mathbf{g}$ is the usual reciprocal lattice vector defined by the fundamental crystallographic unit cell. For a STEM, these vectors must form a fine enough mesh to describe the transverse momentum components of the incident probe and hence are derived from a suitably chosen supercell (Allen et al., 2003). The probe position dependent terms $B^{ij}(\mathbf{R}_0,t)$ are functions of the Bloch state excitations $\alpha^i(\mathbf{R}_0)$ and given by

$$B^{ij}(\mathbf{R}_0,t) = \alpha^i(\mathbf{R}_0)\alpha^{j*}(\mathbf{R}_0)\,\frac{\exp[i2\pi(\lambda^i-\lambda^{j*})t]-1}{i2\pi(\lambda^i-\lambda^{j*})t}. \quad (7)$$

The complex eigenvalue $\lambda^i = \gamma^i + i\eta^i$ accommodates both the quantum splitting of the incident wave vector (via the anpassung γ^i) and absorption of this state via the attenuation factor η^i, mainly due to the thermal diffuse scattering absorption. The excitation amplitudes for a STEM are written as

$$\alpha^i(\mathbf{R}_0) = \sum_{\mathbf{g}} C^{i*}_{\mathbf{g}}\exp(-i2\pi\mathbf{g}\cdot\mathbf{R}_0)\,T(\mathbf{g}), \quad (8)$$

where $T(\mathbf{g})$is the Fourier space representation of the incident probe given by

$$T(\mathbf{g}) = O(\mathbf{g})\exp[-i\chi(\mathbf{g})]. \quad (9)$$

The final terms occurring in equation (6) are the inelastic scattering coefficients $\mu_{\mathbf{h},\mathbf{g}}$, which, in principle, can describe any form of inelastic scattering such as energy-dispersive X-ray analysis, electron-energy-loss spectroscopy, Rutherford backscattering, or, as in the cases considered here, ADF imaging. Using an Einstein model, the inelastic scattering factors for ADF imaging are given by (Allen & Rossouw, 1990)

$$\mu_{\mathbf{h},\mathbf{g}} = \frac{1}{V_c}\sum_n \exp[i2\pi(\mathbf{g}-\mathbf{h})\cdot\boldsymbol{\tau}_n] \times \int\{f_n(\mathbf{q}+\mathbf{g})f_n^*(\mathbf{q}+\mathbf{h})\exp[-M_n(\mathbf{g}-\mathbf{h})] - \exp[-M_n(\mathbf{q}+\mathbf{h})-M_n(\mathbf{q}+\mathbf{g})]\}\,d\Omega, \quad (10)$$

where V_c is the unit cell volume and $\boldsymbol{\tau}_n$ is a vector describing the position of all atoms n with scattering factors $f_n(\mathbf{q})$. The momentum transfer to the crystal is $h\mathbf{q} = h(\mathbf{k}-\mathbf{k}')$, where $\mathbf{k}'$ is the wave vector of the electron scattered into the annular detector described by the angular range $d\Omega$. The Debye–Waller factor is $M_n(\mathbf{q}) = 2\pi^2\langle u_n^2\rangle q^2$, where $\langle u_n^2\rangle$ is the projected mean square thermal displacement.

The Diffractogram

Both incoherent and coherent images are often analyzed by taking their Fourier transforms, the so-called diffractogram,

which provides information about the frequencies contributing to the formation of the image. The incoherent STEM image described in equation (6) is a function of the probe position, $\mathbf{R}_0$, so its diffractogram is written formally as

$$\hat{I}(\mathbf{p}, t) = F[\sigma(\mathbf{R}_0, t)] \equiv \int \sigma(\mathbf{R}_0, t) \exp(-i2\pi\mathbf{p}\cdot\mathbf{R}_0)\, d\mathbf{R}_0, \tag{11}$$

where F denotes a Fourier transform. Noting that the only $\mathbf{R}_0$-dependent part in equation (7) is the Bloch-wave excitation amplitudes and hence the only part that can be Fourier transformed with respect to $\mathbf{R}_0$, we may write

$$\hat{I}(\mathbf{p}, t) = \sum_{i,j} F[\alpha^i(\mathbf{R}_0)\alpha^{j*}(\mathbf{R}_0)] \frac{\exp[i2\pi(\lambda^i - \lambda^{j*})t] - 1}{i2\pi(\lambda^i - \lambda^{j*})t} \times \sum_{\mathbf{g},\mathbf{h}} C_{\mathbf{h}}^{j*} C_{\mathbf{g}}^{i} \mu_{\mathbf{h},\mathbf{g}}. \tag{12}$$

Evaluating the Fourier transform,

$$\begin{aligned} F[\alpha^i(\mathbf{R}_0)\alpha^{j*}(\mathbf{R}_0)] &= \int \alpha^i(\mathbf{R}_0)\alpha^{j*}(\mathbf{R}_0)\exp(-i2\pi\mathbf{p}\cdot\mathbf{R}_0)\, d\mathbf{R}_0 \\ &= \int \Bigg\{ \sum_{\mathbf{g}} C_{\mathbf{g}}^{i*} O(\mathbf{g}) \exp[-i\chi(\mathbf{g})] \exp(-i2\pi\mathbf{g}\cdot\mathbf{R}_0) \\ &\quad \times \sum_{\mathbf{h}} C_{\mathbf{h}}^{j} O^*(\mathbf{h}) \exp[i\chi(\mathbf{h})] \exp(i2\pi\mathbf{h}\cdot\mathbf{R}_0) \\ &\quad \times \exp(-i2\pi\mathbf{p}\cdot\mathbf{R}_0) \Bigg\}\, d\mathbf{R}_0 \\ &= \sum_{\mathbf{g}} C_{\mathbf{g}}^{i*} C_{\mathbf{g}+\mathbf{p}}^{j} O(\mathbf{g}) O^*(\mathbf{g}+\mathbf{p}) \\ &\quad \times \exp[-i\chi(\mathbf{g})] \exp[i\chi(\mathbf{g}+\mathbf{p})]. \end{aligned} \tag{13}$$

It can be noted through comparison that equation (13) contains the OTF integrand expressed in equation (4), indicating the transfer of probe information into the STEM image. Moreover, due to the presence of the $O(\mathbf{g})O^*(\mathbf{g}+\mathbf{p})$ term, it is clear that equation (13), and hence the diffractogram defined in equation (12), is nonzero only if $|\mathbf{p}| \leq 2K_{\max} \equiv p_{\max}$. In other words, in a noise-free imaging system, there are no spatial frequencies in the diffractogram higher than the diameter of the objective aperture. It is important to note that the highest spatial frequency in the STEM image is determined by the objective aperture diameter only, independent of the coherent aberrations in the probe, Bloch-state components $C_{\mathbf{g}}^{i}$, specimen parameters such as thickness t, and even the type of inelastic scattering. All these factors, however, will affect the amplitude of the spots in the diffractogram, a point discussed in more detail in the next section. Similar deduction was performed and the same conclusions were reached in a coherent Bloch-wave model developed by Nellist and Pennycook (1999). Moreover, it is straightforward to show that the same result holds for coherent TEM starting with the definition of the diffractogram for TEM imaging (Ishizuka, 1980). Throughout this article, a modulus has been taken for each diffractogram as a measure of its magnitude.

Results and Discussion

Resolution and Information Transfer

We have shown that the diffractogram $\hat{I}(\mathbf{p}, t)$ contains spatial frequencies up to the cutoff, $p_{\max}$. It is sometimes claimed that the higher the transferred frequencies, the finer are the details in the image and thus the better the resolution (Hänninen, 2002). However, this statement should be used with caution. Generally speaking, a sharper probe, which must have higher frequency components, gives rise to higher resolution. Conversely, due to the aberrations in the electron lens, simply opening the objective aperture or increasing the spatial frequency cutoff does not necessarily result in a sharper STEM probe and hence higher resolution.

As an illustration we examine the relationship between spatial frequencies and resolution using simulated ADF STEM images for Si ⟨112⟩. Figure 1a shows a simulation for a 100-Å-thick crystal using probe parameters typical of the ORNL's aberration-corrected HB603U STEM. The Si dumbbells with atomic columns separated by 0.78 Å are clearly resolved, and the diffractogram (Fig. 1b) shows spatial frequencies out to the cutoff, corresponding to a real-space distance of 0.45 Å. In Figure 1c we simulate the image for the same objective aperture but assume parameters typical of the same microscope prior to aberration correction with $C_s = 1.0$ mm and Scherzer defocus $\Delta f = -572$ Å. The adjacent Si columns are no longer resolved for these parameters. However, frequencies in the diffractogram (Fig. 1d) cover the *same range* as in Figure 1b. Thus, spots in the diffractogram do not directly relate to real resolution, and they only indicate information transferred to the image at different frequencies. Resolution is implicitly contained in the ensemble of the diffractogram spots, but there is no simple relationship between the highest spatial frequency and the resolution. The strongest statement that can be made is that, to resolve a feature of a given size in an image, the existence of spatial frequencies in the diffractogram corresponding to this size is a *necessary but not sufficient condition*. One cannot just rely on how far out information can be obtained in the diffractogram to measure the resolution in an image.

As emphasized in the beginning of this article, any discussion of resolution should be based on the reality of

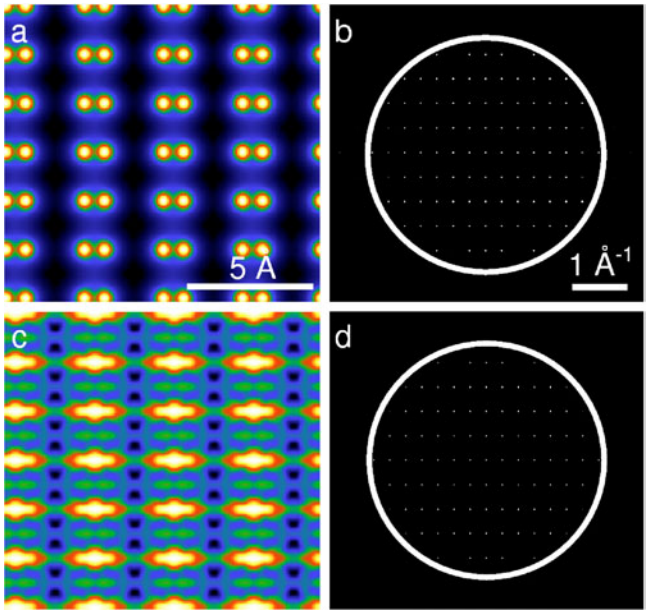

Figure 1. Simulated STEM ADF (detector spanning 90–200 mrad) images and diffractograms for a 100-Å-thick silicon crystal in its ⟨112⟩ zone axis orientation. **a:** Simulated ADF image formed using an aberration-corrected probe with $\Delta f = 20$ Å, $C_s = -0.037$ mm, $C_5 = 100$ mm, and a probe forming aperture of 22 mrad. **b:** Diffractogram corresponding to **a**. **c:** Simulated ADF image formed using uncorrected probe with $\Delta f = -572$ Å, $C_s = 1$ mm and with the same 22-mrad aperture. **d:** Diffractogram corresponding to **c**. White circles represent the cutoff p_{max}, and the maximum values of the diffractograms have been cropped to show the structure within the cutoff.

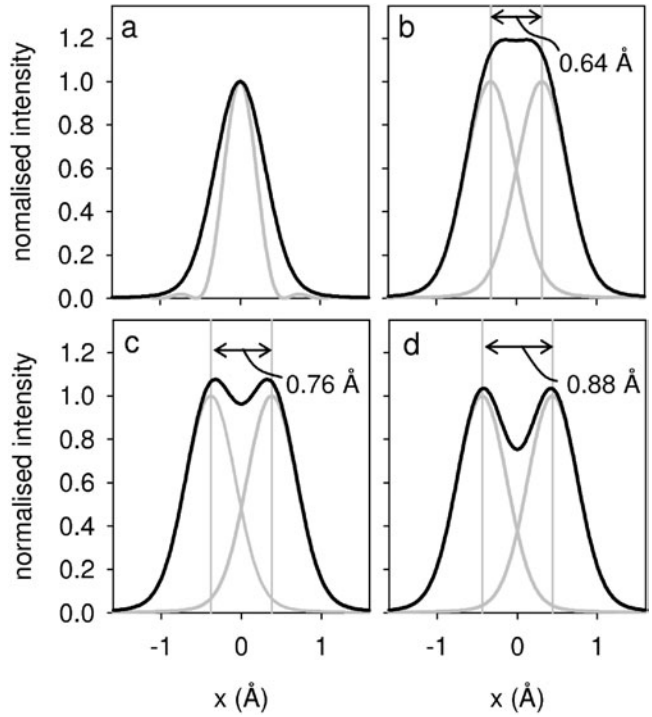

Figure 2. **a:** 300-kV aberration-corrected probe intensity profiles. The gray line shows probe shape accounting for just the coherent aberrations and has FWHM of 0.46 Å. The effect of temporal and spatial incoherence is included by convolution with a Gaussian of 0.60 Å FWHM, resulting in a wider probe of 0.74 Å FWHM (black line). The probe parameters used are objective aperture semi-angle = 22 mrad, $C_s = -0.037$ mm, $\Delta f = 20$ Å, $C_5 = 100$ mm, and the evaluation of Gaussian blur is discussed in a later subsection. Twin probes (gray lines) and their summations (black lines) with a dip contrast of near (**b**) 0%, (**c**) 10%, and (**d**) 27% are shown.

what is observed in the image. We now consider the two-point resolution in more detail. The ability to resolve a two-point object has long been the criterion for defining resolution (Rayleigh, 1879; Sparrow, 1916). A practical measure of the resolvability of two identical objects is the dip contrast (O'Keefe et al., 2005), which can be defined as $C = (I_{peak} - I_{dip})/(I_{peak} - I_{min})$, where, using Figure 1a as an example, I_{peak} is the maximum intensity above the Si column, I_{dip} is the intensity at the midpoint of the Si dumbbell, and I_{min} is the minimum intensity in the entire image. As a simple demonstration, we calculate the probe shape for the aberration-corrected HB603U STEM in Figure 2a. The gray line includes coherent aberrations only. To account for incoherence due to finite source size, defocus spread, and general environmental noise, we have convolved the probe (gray line) with a Gaussian of 0.60 Å FWHM, leading to a blurred probe with a FWHM of 0.74 Å (black line). The reason for the selection of a Gaussian envelope function of this particular size will become apparent in a later section of this article. If we assume pointlike objects with a delta function response to the probe, the ultimate resolution of such an imaging system can be examined in a twin-probe model. In Figure 2b–d we examine the increasing contrast of the summed twin-probe (black line) as the separation between two overlapping probes is increased. Figure 2b corresponds to the Sparrow limit with a contrast of zero and the probes separated by 0.64 Å. In Figure 2c, the contrast is ∼10% with a probe separation of 0.76 Å, and the twin peaks become visibly distinguishable. Figure 2d has a contrast of ∼27%, which corresponds to the Rayleigh criterion for circular apertures. These figures are of course idealized. In practice, real objects have a finite size depending on the type of scattering, the thermal motion of atoms within the sample, and the signal-to-noise ratio of the measurement, possibly lowering the resolution.

Influence of Probe Channeling

Before presenting an experimental image for a more realistic discussion, we briefly examine the probe propagation inside the sample, an important aspect for the correct understanding of resolution in a STEM. The incident probe changes as it propagates through the sample. It is well known that the STEM probe can appear sharper within a

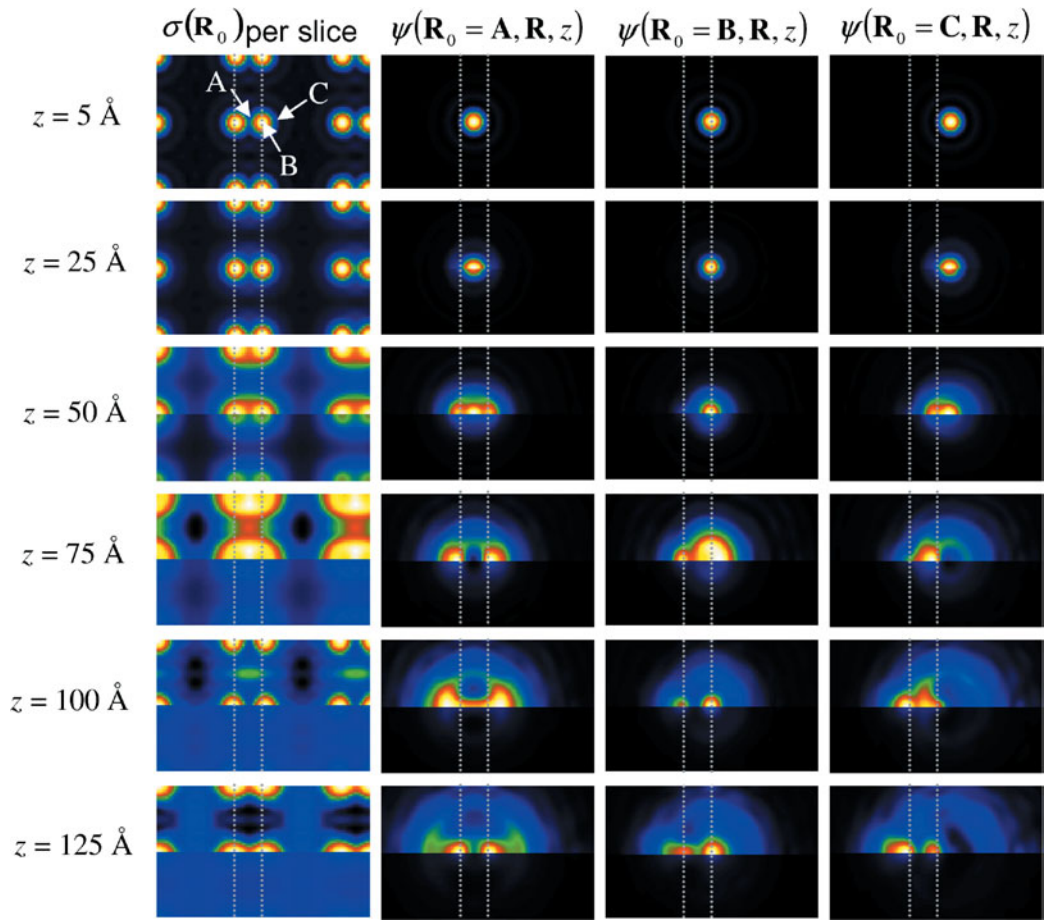

Figure 3. Contributions to the ADF (detector spanning 90–200 mrad) image of Si ⟨112⟩ from individual slices and the corresponding incident electron intensity at each slice for three probe positions. A: The probe located at the midpoint of the Si dumbbells, B: the probe located on the Si column, and C: the probe located just off the Si column. The upper section of each panel is shown on an individual scale to bring out the detail. The lower section is scaled with respect to the maximum for each column in order to indicate the relative strength. The left-hand numbers denote the depth of each slice. The probe parameters are the same as in Figure 2, but the temporal or spatial incoherence is ignored. The dotted lines through the Si columns provide a guide for the eye.

periodic structure than before it hits the crystal (Fertig & Rose, 1981; Dwyer & Etheridge, 2003). This effect occurs with the probe located on an atomic column when the strongly excited 1*s* Bloch state, which is even sharper than state-of-the-art STEM probes (van Aert et al., 2002; Peng et al., 2004), stands out at specific depths as a result of its interference with the non-1*s* states. However, the resultant image will not be sharper than the initial probe. As we will show next, the channeling peak in a crystal *does not move* as the probe is scanned and therefore is *unrelated* to image resolution. The probe function at a depth z in the crystal can be written as $\psi(\mathbf{R}_0, \mathbf{R}, z)$, whereas a STEM image is recorded as a function of probe position $\mathbf{R}_0$. Because we do not record anything as a function of $\mathbf{R}$ in the STEM, the probe shape within a sample for a particular $\mathbf{R}_0$ does not have a direct connection with image resolution. A single pixel in the image corresponds to a single probe position, and this is also why the Fourier transform in equation (11) is with respect to $\mathbf{R}_0$ rather than the lattice point of the specimen, $\mathbf{R}$. In fact, due to the information transfer cutoff imposed by the probe, the resolution of a STEM image is never better than the probe diameter, though it can easily be worse.

The relationship between probe intensity distribution and resolution is illustrated in Figure 3. The leftmost column shows the contribution to the simulated ADF image of Si ⟨112⟩ from each slice at a depth z, and the other three columns show the wave function intensity of the probe within the sample for three selected probe positions **A**, **B**, and **C** as indicated. Each panel consists of two sections; the upper section displays the image contribution or wave function individually scaled to show the detail. The lower section of each panel is scaled using the overall minimum and maximum values of each column to indicate the relative

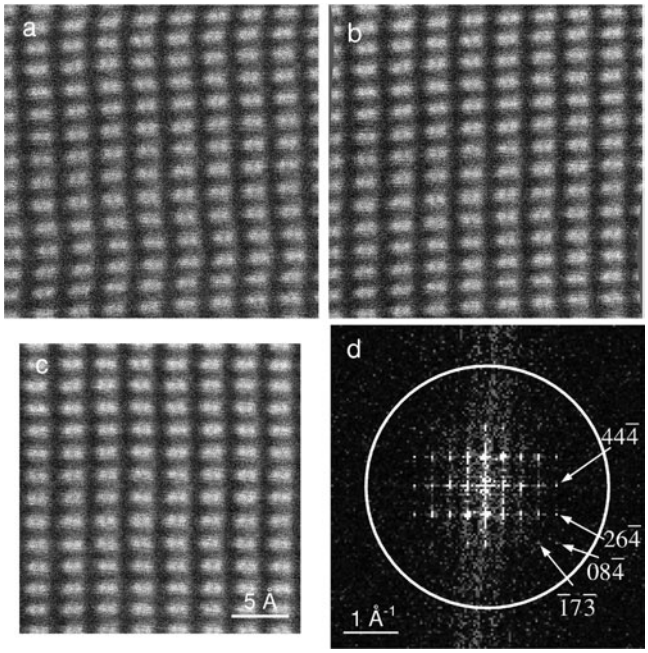

Figure 4. Procedure of image correction prior to extracting the diffractogram. **a:** Colorized raw experimental image of Si ⟨112⟩. **b:** Image from **a** with the wavy distortion removed by linear interpolation. **c:** Image from **b** with the nonorthogonality corrected and then cropped to be strictly periodic. **d:** Diffractogram formed from **c** with the objective aperture indicated by the white circle.

contributions from each depth z. When located over the Si column ($\mathbf{R}_0 = \mathbf{B}$), the probe becomes sharpest at a depth of 25 Å. For all the three distinct probe positions, the probe has spread substantially by a depth of 75 Å, resulting in significantly reduced intensity about the columns. As a result, the contribution to the image mostly comes from the first 75 Å of the sample, with relatively weak contributions from larger depths. In fact, this nodal plane at 75 Å corresponds to the extinction distance due to the interference between the 1s and non-1s Bloch states and agrees very well with the depth oscillation estimation based on a simplified model (Peng et al., 2004). Interestingly, despite the fact that the electron density spreads significantly in the specimen during propagation, the atomic columns are still resolved at all depths except $z = 75$ Å. Nevertheless, it is clear that resolution can only be defined with regard to the probe position $\mathbf{R}_0$ and not simply in terms of the wavefunction of the probe inside the sample.

Experimental Diffractograms and Instabilities

Z-contrast images of Si ⟨112⟩ have been taken with the aberration-corrected HB603U STEM (Nellist et al., 2004). A colorized raw image, which has a wavy feature associated with scan instability, is shown in Figure 4a. With the *a priori* knowledge of a single-crystal Si sample being used, this wavy distortion can be safely removed via linear interpolation (Fig. 4b). Nonorthogonality remaining in Figure 4b due to specimen drift during the scan is unwarped using interpolation and a shearing operation. To avoid possible artifacts introduced by choosing a section of image whose dimensions are not exact integer numbers of lattice spacings, we select a section of the image that has a size of 8 × 13 unit cells. The resulting image (Fig. 4c) is then Fourier transformed to generate the diffractogram (Fig. 4d) for further analysis. The presence of a notable vertical streak extending outside the aperture is due to residual scan instabilities of the probe, and the much weaker speckle outside the aperture is the result of noise in the image. There is also a slight lack of symmetry in the diffractogram, perhaps suggesting a slight tilt away from the ⟨112⟩ orientation.

In an experimental image, several factors can lead to artifactual spots in the diffractogram. First, to confirm that the image signal is not being "clipped" during acquisition (Yu et al., 2003), it is important to check the histogram (Nellist et al., 2004; supporting online material) to ensure that suitable black level and detector gain were used. Second, experimental instabilities can give rise to spots in the diffractogram that are not related to the imaged object, so it is also important to check that spots are not caused by picking a particular scanning speed or direction. Instabilities are undesirable movements of the probe, whether random or periodic over time. The probe position in a STEM image will be a function of time and, as the image points are acquired sequentially, there is a relationship between the frequency of the instability and where it shows up in the diffractogram. An instability that is very much faster than the acquisition time per pixel results in an effective broadening of the probe. Instabilities with frequencies comparable to the pixel time will distort the image. The measurement and removal of systematic distortions from STEM ADF images have been demonstrated recently (Sanchez et al., 2006).

Determination of Specimen Thickness and Probe Defocus

A pressing problem in the field of electron microscopy is the lack of contrast in experimental atomic resolution images when compared to simulation, or the so-called Stobbs factor (Hÿtch & Stobbs, 1994). If we assume that the lack of contrast can be treated by adding a constant background, then varying the strength of the zero-order peak in the diffractogram of a simulated image allows direct adjustment of contrast. What is encoded in all the other spots in the diffractogram, according to equations (12) and (13), is the information about sample thickness and probe defocus. The variation in the relative intensities of spots in simulated Si ⟨112⟩ diffractograms is plotted in Figure 5 as a function of specimen thickness t and defocus Δf. A total of 17 strong reflections are used and identified in Table 1 with the zero-order reflection ignored. For a thin specimen of 10 Å, a strong variation of the intensity distribution is seen as a

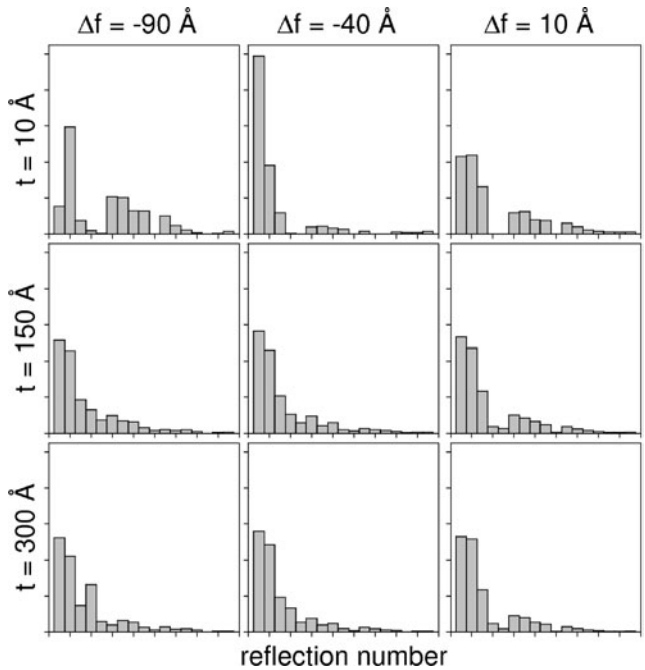

Figure 5. Variation of the first 17 reflections in the diffractogram with varying defocus (left to right) and specimen thickness (top to bottom) for simulated Si ⟨112⟩ images.

function of defocus, and the variation becomes weaker for thicker specimens. There is also a redistribution of intensity as a function of thickness for fixed defocus. This variation can be used to determine the probe defocus and specimen thickness in combination with image simulations using a linear regression technique. For a more realistic description, a parameter for Gaussian blur is introduced to account for chromatic effects and the source size. The best fit can be obtained by minimizing the sum squared error, which is a function of defocus, thickness, and Gaussian blur and can be written as

$$\chi^2 = \sum_{\mathbf{p}} [a \times \hat{I}_{\text{theory}}(\mathbf{p}) + b - \hat{I}_{\text{exp}}(\mathbf{p})]^2, \tag{14}$$

where a and b are fitting parameters.

To extract the experimental reflections that have a diffuse distribution, we choose a square patch with a pixel size of 5×5 centered on each reflection in the diffractogram and take the root sum square over this selected region (Loane et al., 1992). The experimental noise, which is estimated as follows, is then removed from the extracted fringe magnitudes. We note that noise in a STEM diffractogram has a reduced distribution with increasing spatial frequency $|\mathbf{p}|$. Thus, the noise level is evaluated statistically in an annular region located at a given $|\mathbf{p}|$ with a radial width of 5 pixels. To rule out artifacts from the instability-related vertical stripe, we limit the selected annular region to an angular range of $[-\pi/3, \pi/3]$. In addition, strong pixels corresponding to apparent reflection signals are also excluded from the annular area prior to the noise analysis. Based on the statistics for the noise histogram at a given $|\mathbf{p}|$, the probability of a reflection at this specific $|\mathbf{p}|$ to be a real signal can be measured in terms of a confidence level, which is evaluated by the cumulative probability corresponding to the reflection magnitude in the noise histogram. The $44\bar{4}$ spot, which corresponds to the smallest atomic-column spacing of 0.784 Å, has a confidence level of 97% and can be clearly observed. Because this dumbbell spacing is distinctly resolved, spots corresponding to higher spatial frequencies and hence smaller length scales are expected to be present. In particular, the $26\bar{4}$ reflection at 0.726 Å has a 95% confidence level and the $\bar{1}7\bar{3}$ reflection at 0.707 Å has 92% confidence. There is also a weak $08\bar{4}$ spot at 0.607 Å with a confidence level of 71%, which is very close to the noise level, and can thus be defined as the effective information limit in this case. It is clear that the range of frequencies contained in the diffractogram is not only limited by the objective aperture, but also by noise, which reduces the effective cutoff for information transfer to the image.

We now examine the fitting results. The contour plot in Figure 6a indicates that the defocus is well defined as −45 Å with an accuracy of about ±5 Å. However, the thickness has a broad range from ∼200 Å to ∼400 Å. With a fixed defocus at −45 Å, Figure 6b shows that the Gaussian blur can be estimated to be 0.60 ± 0.05 Å. Compared to Figure 6a, Figure 6b provides similar information for the distribution of specimen thickness. To narrow down the thickness range, one can refer to the bright-field STEM image taken simultaneously with the ADF image. At a

Table 1. First 17 Reflections in the Diffractogram of Si ⟨112⟩ as Used in Figure 5

No.	*hkl*	p (Å^{-1})	r (Å)
1	$11\bar{1}$	0.319	3.316
2	$\bar{2}20$	0.521	1.920
3	$\bar{1}3\bar{1}$	0.611	1.638
4	$22\bar{2}$	0.638	1.568
5	$04\bar{2}$	0.823	1.214
6	$33\bar{3}$	0.957	1.045
7	$\bar{4}40$	1.042	0.960
8	$15\bar{3}$	1.089	0.918
9	$\bar{3}5\bar{1}$	1.089	0.918
10	$\bar{2}6\bar{2}$	1.221	0.819
11	$44\bar{4}$	1.276	0.784
12	$26\bar{4}$	1.378	0.726
13	$\bar{1}7\bar{3}$	1.414	0.707
14	$\bar{6}60$	1.562	0.640
15	$55\bar{5}$	1.595	0.627
16	$\bar{5}7\bar{1}$	1.595	0.627
17	$08\bar{4}$	1.647	0.607

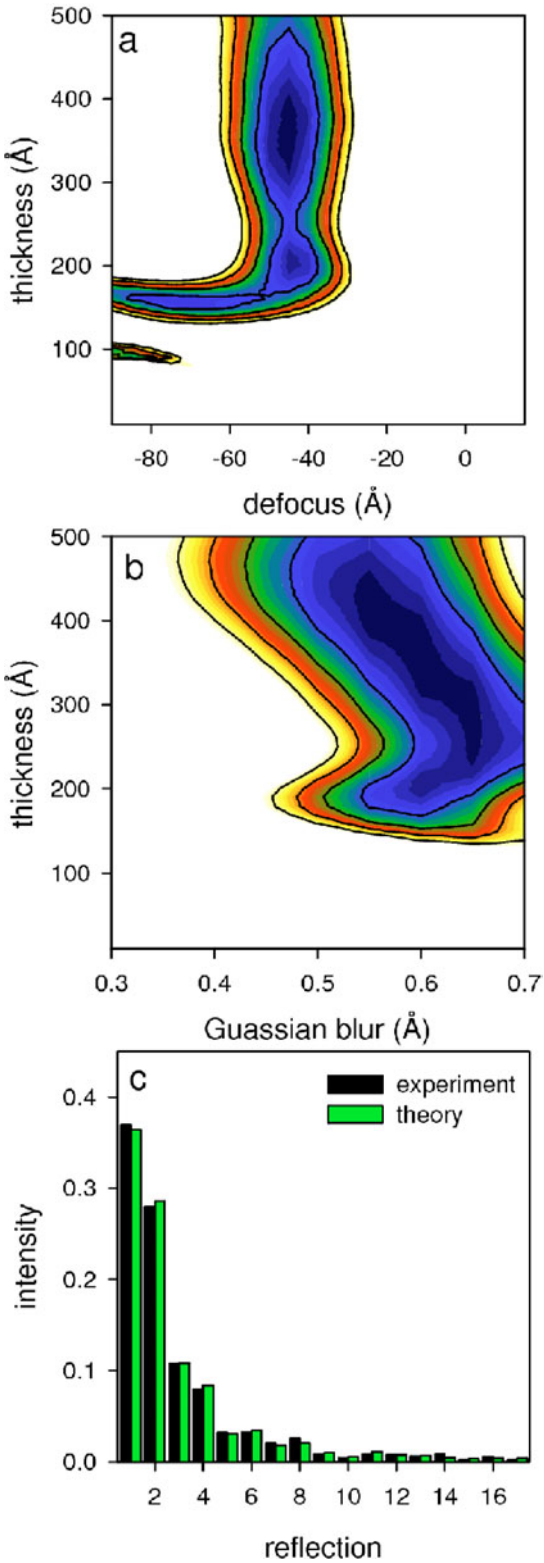

Figure 6. **a:** Contour plot of the sum-squared error versus defocus and thickness for a fixed Gaussian blur of 0.60 Å. **b:** Contour plot of the sum-squared error versus Gaussian blur and thickness for a fixed defocus of −45 Å. **c:** The determined best fit between the 17 simulated and experimental reflections in the diffractogram, with estimated thickness of 300 Å. The two sets of reflections have been normalized by their respective sum.

defocus of −45 Å, simulations of Si ⟨112⟩ phase contrast images show that there exists a contrast reversal, with atoms appearing in black when the thickness is increased to near 400 Å. Because the atoms in the experimental bright field image (not shown here) appear in white contrast, we choose a minimum in Figure 6a,b away from the thickness area near 400 Å. A value of 300 Å appears to be a good choice for the thickness, and the simulated reflections are then compared with experimental results in Figure 6c. Simulations also suggest that, for a silicon sample thinner than about 100 Å, its thickness can be well determined to an accuracy of ∼10 Å, but much worse for thicker specimens. Conversely, the defocus value can be very well defined in the case of thick silicon samples above ∼100 Å, but the accuracy decreases for thinner samples because the scattering of an incident probe by a thin specimen is relatively insensitive to the defocus values. A future improvement with this Fourier-space approach is to make use of an experimental focal series of bright- and dark-field images taken for the same thickness, which would not only provide a robust test of the determined defocus through fitting, but also possibly ameliorate the low accuracy for specimen thickness estimation.

A subsection of the experimental ADF image from Figure 4c is shown in Figure 7a, and Figure 7b shows a simulation of the ADF image using the parameters stated in the caption. It is important to realize that the diffractogram contains information about the entire image, not just any individual dumbbell. We have averaged over all 96 dumbbells in the image to account for this, taking line scans 10 pixels wide. A comparison of the averaged experimental dumbbell line scans with theory (also averaged over a width of 10 pixels) is shown in Figure 7c. There is excellent agreement between the simulated and experimental dumbbell profile, which has a dip contrast of 11% for the distinctly resolved Si dumbbell. For a practical measure of resolution, it appears appropriate to adopt a standard in between the Rayleigh and Sparrow criteria. We propose a two-peak distance with a central dip contrast of 10%. We note that there is generally a small increase from the left to right column in each dumbbell, possibly due to a slight tilt and the sample not being precisely in the zone-axis orientation. Moreover, in order to obtain similar contrast, the simulation has been matched to the experiment by adding a constant background, which corresponds to adjusting the strength of the zero spot in the diffractogram of the experimental image.

Ultimate and Optimum Resolution

Before concluding, we briefly discuss the ultimate resolution limit for *Z*-contrast STEM. For a weakly scattering object, it has been shown that the ADF detector selects only the high order Fourier components of the potential, and the incoherent image is given by a convolution between the high-pass filtered potential and the point-spread function

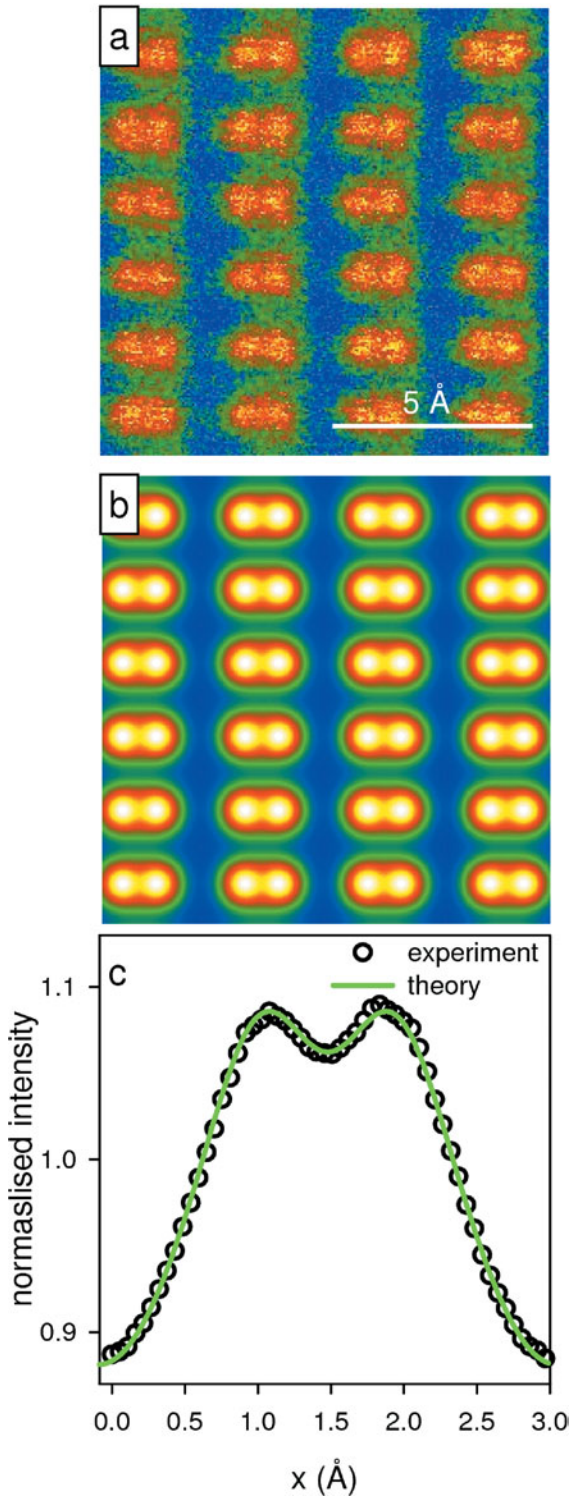

Figure 7. a: Subsection of experimental ADF image of Si ⟨112⟩ using detector spanning 90–200 mrad. **b:** Simulated image for t = 300 Å, Δf = −45 Å, C_s = −0.037 mm, C_5 = 100 mm, and probe-forming aperture of 22 mrad. Temporal and spatial incoherence have been accounted for by convolving with a Gaussian with FWHM of 0.60 Å. **c:** Line scans averaged over width of 10 pixels comparing experiment and theory. The experimental result has been averaged over a total of 96 dumbbells and normalized by the average of the data points shown.

(Pennycook & Nellist, 1999). In principle at least, the resolution limit for ADF STEM is higher than that for bright-field imaging. The effective potential in Z-contrast imaging is the inelastic potential filtered by the ADF detector, whereas the effective potential is the elastic potential for bright-field STEM or conventional TEM imaging (Fig. 8a). The ADF potential has a much reduced background and sharper peaks due to the high-pass filtering (Fig. 8b). Increasing the ADF detector inner angle gives rise to even narrower potential peaks (Fig. 8c), effectively making the atoms smaller. With adjustable object size, one can immediately see the resolution advantage of STEM ADF imaging over TEM. It should be noted that thermal vibration has a broadening effect on the size of the atoms (O'Keefe et al., 2005). This blurring of the atomic potential cannot be reduced by any filtering, only by reducing the specimen temperature as illustrated by the gray lines in Figure 8, which show the potentials for T = 100 K. The effective atom size, which can be reduced by increasing the inner angle of the ADF detector, is now an important element affecting resolution. The next generation aberration-corrected STEMs (e.g., Krivanek et al., 2003) will provide sharper probes although still larger than the typical size of scattering potentials in materials. It will be interesting to see if the width of the atom potential forms the ultimate limit on the resolution, as predicted by Beck and Crewe (1975), or whether noise remains the limiting factor. An optimum detector angle should exist where the improved resolution due to reduction of atom size is offset by the reduced signal and information transfer due to noise.

Conclusions

In a dynamical theory of incoherent imaging of a crystal, we have used an analytical derivation to clarify the relation between information transfer and resolution. The former is shown to be a necessary but not sufficient condition for achieving the latter, corresponding to the same spatial frequency. Resolving capability is addressed in the framework of the two-point resolution, and a practical criterion for resolution is proposed based on the central dip contrast of the two-point object being 10%. Because a single STEM probe position corresponds to a single pixel in the image, the image contrast, and thus resolution, cannot be directly linked to or interpreted in terms of the wavefunction intensity within the sample for a given probe location. The range of information transfer to a STEM image is determined by the objective aperture, although noise and instabilities reduce the effective limit. The sample thickness and probe defocus are evaluated through linear fitting in Fourier space, and a quantitative comparison between experimental and simulated image is obtained with very good agreement. For a thin silicon sample, its thickness can be well determined but with only rough accuracy for the defocus. For thicker

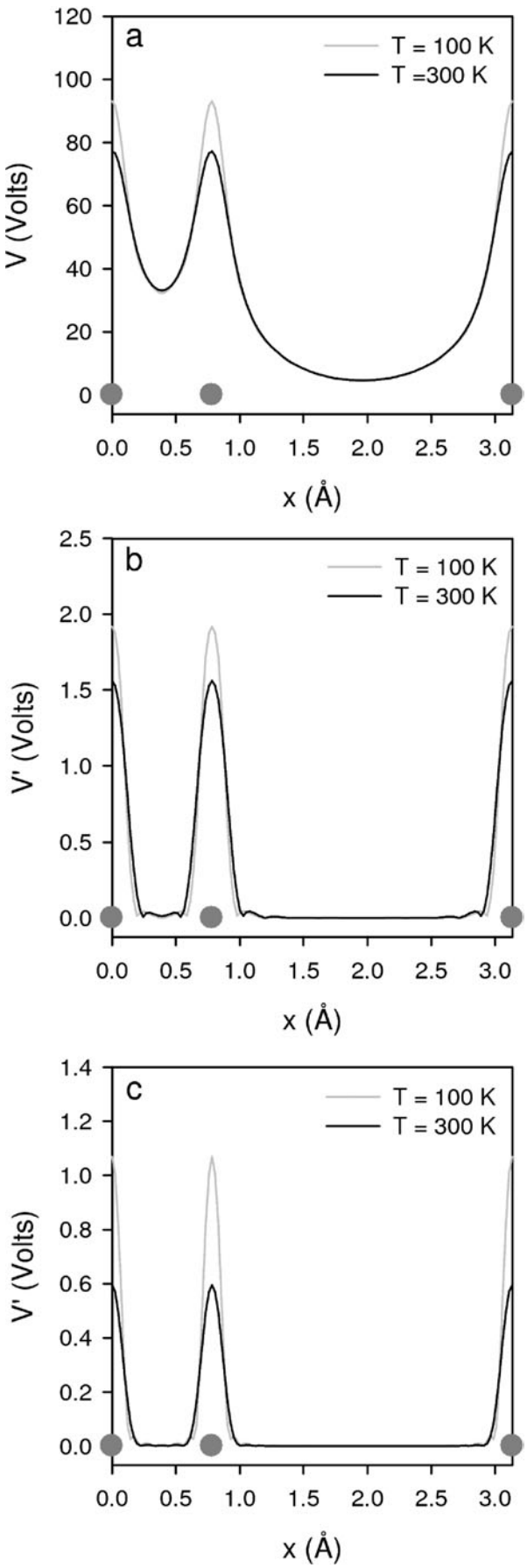

silicon specimens, the defocus value can be very well determined, but the thickness is not as well defined. As the inner angle of the ADF detector is increased, the width of the scattering potential reduces, effectively making the atoms smaller than seen in bright field imaging. The increased noise can also limit the information transfer and an optimum detector angle exists dependent on the specimen.

Acknowledgments

This research was sponsored by the Office of Basic Energy Sciences, Division of Materials Sciences and Engineering, U.S. Department of Energy, under contract DE-AC05-00OR22725 with Oak Ridge National Laboratory, managed and operated by UT-Battelle, LLC, and by (Y.P., M.P.O.) appointment to the ORNL Postdoctoral Research Program administered jointly by ORNL and ORISE.

References

Allen, L.J., Findlay, S.D., Oxley, M.P. & Rossouw, C.J. (2003). Lattice-resolution contrast from a focused coherent electron probe. Part I. *Ultramicroscopy* **96**, 47–63.

Allen, L.J. & Rossouw, C.J. (1990). Absorptive potentials due to ionization and thermal diffuse scattering by fast electrons in crystals. *Phys Rev B* **42**, 11644–11654.

Beck, V. & Crewe, A.V. (1975). High resolution imaging properties of the STEM. *Ultramicroscopy* **1**, 137–144.

Dellby, N., Krivanek, O.L., Nellist, P.D., Batson, P.E. & Lupini, A.R. (2001). Progress in aberration-corrected scanning transmission electron microscopy. *J Electron Microsc* **50**, 177–185.

Den Dekker, A.J. & Van Den Bos, A. (1997). Resolution: A survey. *J Opt Soc Am A* **14**, 547–557.

Dwyer, C. & Etheridge, J. (2003). Scattering of Å-scale electron probes in silicon. *Ultramicroscopy* **96**, 343–360.

Fertig, J. & Rose, H. (1981). Resolution and contrast of crystalline objects in high-resolution scanning transmission electron microscopy. *Optik* **59**, 407–429.

Findlay, S.D., Allen, L.J., Oxley, M.P. & Rossouw, C.J. (2003). Lattice-resolution contrast from a focused coherent electron probe. Part II. *Ultramicroscopy* **96**, 65–81.

Haider, M., Uhlemann, S., Schwan, E., Rose, H., Kabius, B. & Urban, K. (1998). Electron microscopy image enhanced. *Nature* **392**, 768–769.

Hänninen, P. (2002). Beyond the diffraction limit. *Nature* **419**, 802.

Figure 8. Profiles of projected Si ⟨112⟩ crystal potentials at different temperatures. (**a**) Elastic potential, (**b**) inelastic potential filtered by ADF detector of 45–200 mrad, and (**c**) 90–200 mrad. Small oscillations in **b** and **c** are due to incomplete convergence of the Fourier series of inelastic scattering coefficients, which does not appreciably affect the width of these potentials.

Hÿtch, M.J. & Stobbs, W.M. (1994). Quantitative comparison of high-resolution TEM images with image simulations. *Ultramicroscopy* **53**, 191–203.

Ishizuka, K. (1980). Contrast transfer of crystal images in TEM. *Ultramicroscopy* **5**, 55–65.

Kirkland, E.J. (1998). *Advanced Computing in Electron Microscopy*. New York: Plenum Press.

Krivanek, O.L., Nellist, P.D., Dellby, N., Murfitt, M.F. & Szilagyi, Z. (2003). Towards sub-0.5 Å electron beams. *Ultramicroscopy* **96**, 229–237.

Loane, R.F., Xu, P. & Silcox, J. (1992). Incoherent imaging of zone axis crystals with ADF STEM. *Ultramicroscopy* **40**, 121–138.

Nellist, P.D., Chisholm, M.F., Dellby, N., Krivanek, O.L., Murfitt, M.F., Szilagyi, Z.S., Lupini, A.R., Borisevich, A., Sides, W.H. & Pennycook, S.J. (2004). Direct sub-Angstrom imaging of a crystal lattice. *Science* **305**, 1741.

Nellist, P.D. & Pennycook, S.J. (1999). Incoherent imaging using dynamically scattered coherent electrons. *Ultramicroscopy* **78**, 111–124.

O'Keefe, M.A. & Allard, L.F. (2004). A standard for sub-Ångström metrology of resolution in aberration-corrected transmission electron microscopes. *Microsc Microanal* **10**(suppl. 2), 1002–1003.

O'Keefe, M.A., Allard, L.F. & Blom, D.A. (2005). HRTEM imaging of atoms at sub-Ångström resolution. *J Electron Microsc* **54**, 169–180.

Peng, Y., Nellist, P.D. & Pennycook, S.J. (2004). HAADF-STEM imaging with sub-angstrom probes: A full Bloch wave analysis. *J Electron Microsc* **53**, 257–266.

Pennycook, S.J. & Nellist, P.D. (1999). Z-contrast scanning transmission electron microscopy. In *Impact of Electron and Scanning Probe Microscopy on Materials Research*, Rickerby, D.G., Valdrè, G. & Valdrè, U. (Eds.), pp. 161–207. Boston, MA: Kluwer Academic Publishers.

Rayleigh, Lord (1879). Investigations in optics, with special reference to the spectroscope. *Philos Mag* **8**, 261–274, 403–411, 477–486.

Sanchez, A.M., Galindo, P.L., Kret, S., Falke, M., Beanland, R. & Goodhew, P.J. (2006). An approach to the systematic distortion correction in aberration-corrected HAADF images. *J Microsc* **221**, 1–7.

Scherzer, O. (1949). The theoretical resolution limit of the electron microscope. *J Appl Phys* **20**, 20–29.

Sparrow, C.M. (1916). On spectroscopic resolving power. *Astrophys J* **44**, 76–86.

Van Aert, S., Den Dekker, A.J., Van Dyck, D. & Van Den Bos, A. (2002). Optimal experimental design of STEM measurement of atom column positions. *Ultramicroscopy* **90**, 273–289.

Van Dyck, D., Van Aert, S. & Den Dekker, A.J. (2004). Physical limits on atomic resolution. *Microsc Microanal* **10**, 153–157.

Yu, Z., Batson, P.E. & Silcox, J. (2003). Artifacts in aberration-corrected ADF-STEM imaging. *Ultramicroscopy* **96**, 275–284.